Effects of interface cohesion on mechanical properties of interpenetrating phase nanocomposites

Xiao-Yu Sun[1], *Guang-Kui Xu*[2], *Jun-Hui Zhang*[3], *Yuan-Jie Xu*[1]

[1]*Department of Engineering Mechanics, School of Civil Engineering, Wuhan University, Wuhan 430072, People's Republic of China*
[2]*International Center for Applied Mechanics, State Key Laboratory for Strength and Vibration of Mechanical Structures, Xi'an Jiaotong University, Xi'an 710049, People's Republic of China*
[3]*Department of Civil Engineering, North China University of Technology, Beijing 100144, People's Republic of China*
E-mail: xiaoyusun@whu.edu.cn

Published in Micro & Nano Letters; Received on 30th May 2014; Revised on 31st July 2014; Accepted on 18th August 2014

Molecular dynamics simulations and micromechanics model analysis are performed to investigate the mechanical behaviours and interfacial effects of interpenetrating phase composites in the nanoscale. It is observed that the overall Young's modulus and ultimate strength of the nanocomposites vary nonlinearly with the cohesive energy of the interface. The cohesive properties affect the stiffness of the interface zone, and in turn, influence the effective Young's modulus of composites. The competition between interfacial failure and weak phase damage results in an optimal cohesive parameter of the interface, at which the composite possesses the maximal ultimate strength. The obtained results provide useful guidelines for the design and optimisation of advanced nanocomposites with superior mechanical properties.

1. Introduction: In the past decade, the interpenetrating phase composite (IPC) has attracted much attention for its unique topological microstructure. These structures are observed in many biological materials such as bones and deer antlers [1], and enable these materials to fulfil their biological functions. In such composites, the composed phases are each spatially continuous and interconnected in three dimensions. If one of the constituent phases is removed from the IPC, the remaining material forms an open-celled foam, which can still support loading alone [2–4]. Owing to this continuously interpenetrated structure, IPCs possess some unexpected physical and mechanical properties, such as high yield strength and charge-induced reversible strain, which are evidently superior to conventional particle or fibre-reinforced composites [5, 6]. These properties make IPCs promising candidates for potential application in a variety of fields, such as wear-resisting materials, high-performance energy absorption, ultrastrength materials and three-dimensional (3D) printing [7–11].

A number of theoretical and experimental efforts have been directed towards investigating the overall mechanical behaviours (e.g. elastic modulus, strength, fracture toughness and energy dissipation) of IPCs [3, 4, 12–14]. For example, Wegner and Gibson [14] experimentally examined the fracture toughness of two composites with interpenetrating phase morphologies and various volume fractions. They observed that cracks follow a tortuous path, and prefer to travel through the weaker phase as well as the interfaces. Feng *et al.* [3, 4] proposed a micromechanics cell model, and calculated the effective elastic moduli and elastoplastic constitutive relations of IPCs. On the basis of several analytical models and numerical approaches, Poniznik *et al.* [12] proposed the most appropriate method to estimate the effective elastic properties of metal–ceramic IPCs. Agarwal *et al.* [13] presented unit cell and self-consistent models to investigate the elastic properties of IPCs, and analysed these models by the element-free Galerkin method. The macroscopic mechanical response of the composite is sensitive to its interfacial properties. Previous research on the interface effect of microcomposites has focused on how to propose appropriate cohesive zone models (CZMs) to describe the discrete fracture processes of the interface [15]. CZMs can be used to simulate a wide range of fracture processes in a variety of composite systems. Various functional forms of traction–separation equations and the related parameters for different CZMs have been discussed. It is found that for a specific composite system, this model relies on carefully designed and conducted experiments to select a proper form and related parameters [16, 17].

Despite the progress towards an understanding of the mechanical behaviours of IPCs, previous studies have mainly focused on the microscale structure. However, when an IPC shrinks to the nanoscale, the nanocomposite possesses a large number of interfaces. The atomic-level mechanism remains unclear as to how the cohesive properties (e.g. cohesive strength and cohesive energy) of these interfaces affect the overall mechanical properties of IPCs in the nanoscale. In this Letter, we perform molecular dynamics (MD) simulations to study the overall mechanical behaviours of IPCs with various cohesive properties of interface subjected to uniaxial tension. Moreover, we propose a micromechanics model to investigate the relationship between the nanoscale properties of interfaces and the macroscopic behaviours of nanocomposites. It is demonstrated that the cohesive properties of the interface are critical in capturing the overall mechanical behaviours of IPCs.

2. Methods: In our study, we choose the aluminium–silicon composite and the random bicontinuous network microstructure as our model system. Aluminium–silicon composite is widely used in many significant fields such as aerospace and aviation, and it is an ideal candidate for studying the deformation feature of nanocomposites [18, 19]. The random bicontinuous network microstructure is the most common structure of IPCs. We construct this structure by using the phase field method, which can simulate the spinodal decomposition process of a binary fluid mixture [20, 21]. During spinodal decomposition, the fluid mixture, with its two components uniformly distributed at the initial state, will decompose into two phases spontaneously. It has been found that the morphology of spinodally decomposed binary mixtures is similar to the morphology of IPCs [22]. The evolution of the spinodal microstructure can be described by the Cahn-Hilliard equation [23, 24]. After spinodal decomposition, the two separated phases are replaced by single-crystalline aluminium and silicon, respectively [25].

The initial configuration of the simulation model is shown in the inset of Fig. 1. In the simulations, the volume ratio of aluminium

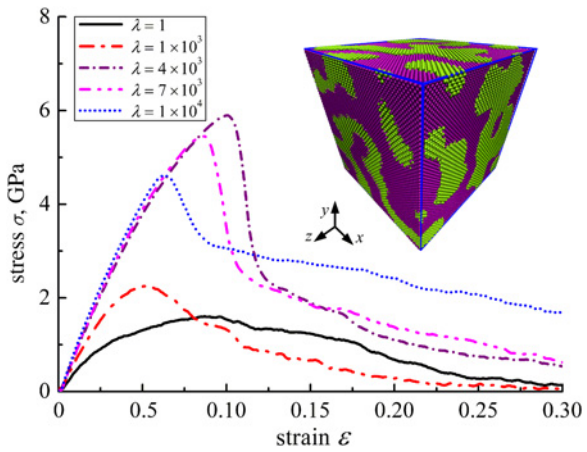

Figure 1 *Tensile deformation behaviours of the nanocomposites with cohesive parameter λ varying from 1 to 1 × 10^4*
Inset: Atomic configuration of an interpenetrating phase nanocomposite sample
Al and Si atoms are painted in purple and light yellow colours, respectively

and silicon was set as 1:1. The representative volume element (RVE) with a cuboid shape of $20 \times 20 \times 20$ nm^3 in size was simulated by using LAMMPS [26]. Periodic boundary conditions were imposed in all three directions. After the initial construction, the conjugate gradient method was used to obtain equilibrium configurations by minimising the system energy. Then, a uniaxial tensile loading along the *y*-direction was performed by stretching the simulation box. In each loading step, the distances between atoms were increased at an engineering strain of 0.1%, and then the configuration was relaxed for 1 ps at a constant temperature of 300 K using a Nose-Hoover thermostat. The time step was set at 1 fs. The atomic stresses were calculated using the Virial theorem [27], and the macroscopic stress was obtained by averaging all atomic stresses over the last 50 time steps of the relaxation period at each loading step.

The interactions between Si atoms were simulated using the Tersoff three-body potential [28]. An empirical embedded-atoms method (EAM) potential developed by Zope and Mishin [29] was used to describe the interaction between Al atoms, which is calibrated according to the *ab-initio* values of twin and stacking fault formation energies. Actually, the atom interactions in the interface zone are complicated, because the organic binding agents are often used between two composed phases in composites [30]. The cohesive strength and cohesive energy of the interface could be affected through changing the amount, content and concentration of binding agents.

There are many potentials used to describe the interactions between Al and Si atoms. The modified embedded atom method (MEAM) potential is an attractive choice to model Al–Si composite [31]. This potential is improved based on the EAM potential, and can be obtained by fitting to some physical properties such as bulk modulus, lattice parameter and cohesive energy, which are computed by a local density approximation (LDA) method [32]. The MEAM potential allows for the crystal orientation dependence of the silicon bonding and includes second nearest-neighbour (2NN) effects for aluminium [33]. However, the MEAM potential has a cutoff mechanism in its many-body angular screening function, which makes this simulation potential computationally expensive. To incorporate the angular dependence with a unified functional form, an angular-dependent embedded atom method (A-EAM) potential for mixed metal–covalent systems has been developed [34, 35]. This potential is formulated by combining the EAM potential for aluminium with the Stillinger-Weber (SW) potential for silicon. By taking advantage of both EAM and SW potentials, the A-EAM potential can provide an accurate and efficient description of the mechanical properties of the metal–covalent composite. In addition, the Lennard-Jones (LJ) potential is also generally applied to describe the interaction for mixed metal–covalent systems in MD simulation since it can be easier to implement [36–38]. In this Letter, we mainly consider the influence of relative interface cohesion. So a compromise is taken to choose the LJ force field. Despite this potential being not the most precise, it allows for extracting the physics of the problem. For the LJ potential, the energy between two atoms is $U_{LJ}(r) = 4\varepsilon[(\sigma/r)^{12} - (\sigma/r)^6]$, where ε is the depth of the potential well, r is the distance between two atoms and σ is the distance at which the potential is zero [37]. For interactions between Al–Si atoms without the binding agents, Peng *et al.* [36] obtained the parameters $\varepsilon_0 = 0.0262$ meV and $\sigma_0 = 3.223$ Å using the Lorentz and Berthelot mixing rules. The potential well depth ε, to some extent reflects the cohesive properties of the interface. To investigate the dependence of the overall mechanical properties of the constructed IPC on the cohesive properties of the interface, a series of MD simulations were performed. In the simulations, all samples had the same $\sigma = \sigma_0$ but different potential well depth values $\varepsilon = \lambda\varepsilon_0$, where λ is defined as the cohesive parameter. The cohesive strength and cohesive energy are proportional to the cohesive parameter [39, 40]. A large value of λ means relative higher cohesive strength and cohesive energy.

3. Results and discussion

3.1. Stress–strain curves: Fig. 1 shows the typical tensile stress–strain curves for the IPC with various cohesive parameters. All the samples show a nearly linear stress–strain response at the initial deformation stage. Then, as the strain increases, the stresses further increase with a nonlinear plastic relationship. This plastic behaviour of the IPC is attributed to the dislocation slip, and stacking faults accumulate in Al [41]. In this Letter, the maximum stress value is defined as the overall ultimate tensile strength σ_u. Beyond this maximum, the stress–strain curves exhibit a negative slope, meaning that failure of the IPC occurs.

The Young's modulus E and the ultimate strength σ_u of a given IPC sample are measured from the stress–strain curves and plotted in Fig. 2. As shown in Fig. 2*a*, the capacity of elastic deformation of the IPC is significantly enhanced with the increase of the cohesive parameter λ when $\lambda < \lambda_c = 4 \times 10^3$. For example, the Young's modulus E increases by 125.6%, from 36.3 to 81.9 GPa, as λ changes from 1 to λ_c. However, the Young's modulus displays slight change if λ is larger than λ_c. Fig. 2*b* illustrates the dependence of the ultimate strength σ_u of the nanocomposite on λ. In the case of $\lambda < 1 \times 10^2$, σ_u remains nearly a constant (1.6 GPa), and shows slight dependence on λ. As λ increases from 1×10^3 to 4×10^3, σ_u shows a pronounced increase from 2.3 to 5.9 GPa, corresponding to a relative change of about 156.5%. As the cohesive parameter λ further increases, the overall ultimate strength decreases, indicating that there is an optimal cohesive parameter $\lambda_c = 4 \times 10^3$ at which the composite possesses the maximum ultimate strength.

In our simulation, the average characteristic size of aluminium/silicon nanocomposite was ~10 nm. The effective Young's modulus of the nanocomposite ranges from 36.3 to 81.9 GPa, and the strength ranges from 1.6 to 5.9 GPa. The mechanical properties of aluminium/silicon in the microscale have been measured by four-point flexural strength tests [42–44]. For the aluminium/silicon microcomposites with a characteristic size of ~10 μm and with different silicon volume fractions, the effective Young's modulus ranges from 1.74 to 3.22 GPa, and the average strength ranges from 116.7 to 170.2 MPa. Both the Young's modulus and the strength of the nanocomposites are an order of magnitude higher than those of microcomposites, indicating that the nanocomposites are much stronger. The mechanical properties of nanocomposites differ from the conventional microcomposite materials because of the superhigh interface-to-volume ratio.

3.2. Failure mechanisms: To reveal the physical mechanisms underlying the observed deformation behaviours, the

doi: 10.1049/mnl.2014.0304

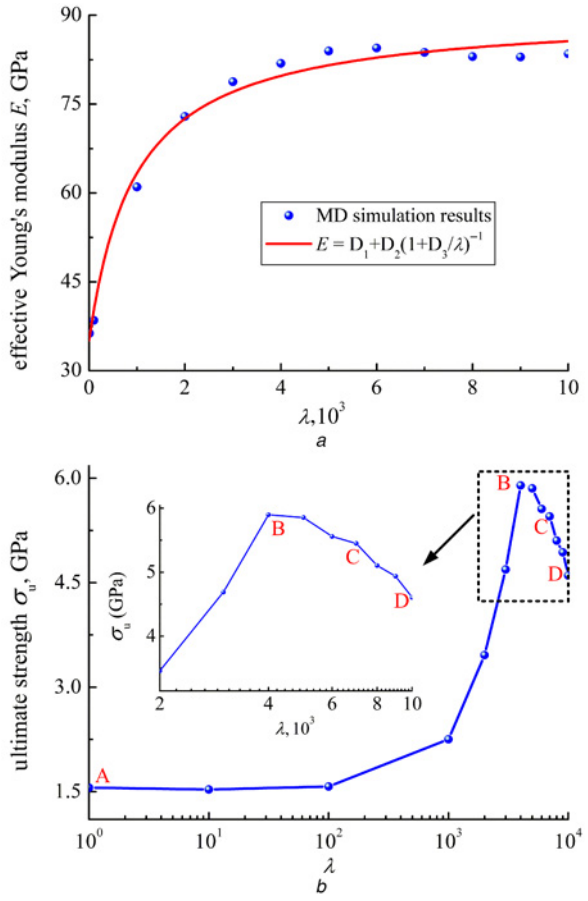

Figure 2 *Mechanical properties of IPC*
a Effective Young's modulus of IPC against λ, with a comparison between the MD simulation and micromechanics methods
b Relationship between the ultimate strength σ_u and the cohesive parameter λ of IPC
Points A, B, C and D corresponding to $\lambda = 1$, $\lambda = 4 \times 10^3$, $\lambda = 7 \times 10^3$ and $\lambda = 1 \times 10^4$, respectively
Inset: Enlarged view of the $\sigma_u \sim \lambda$ curves at higher values of λ

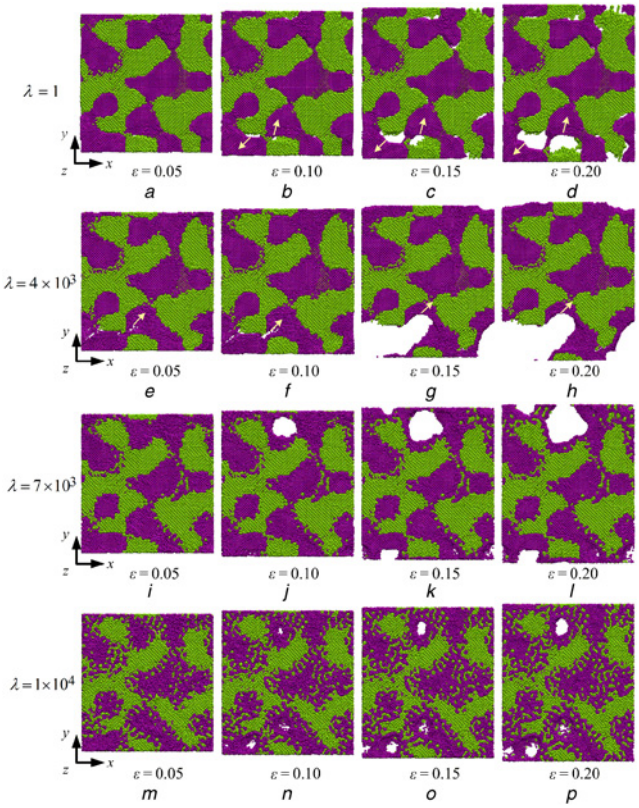

Figure 3 *Evolution of microstructures in IPC samples with different cohesive parameters*
a–d $\lambda = 1$
e–h $\lambda = 4 \times 10^3$
i–l $\lambda = 7 \times 10^3$
m–p $\lambda = 1 \times 10^4$
Loading direction is along the *y*-axis

microstructural evolution during deformation was investigated. Fig. 3 presents a sequence of snapshots of four typical IPCs with different values of λ. Al and Si atoms are painted in purple and light yellow colours, respectively.

When λ is smaller (e.g. $\lambda = 1$), the microstructural evolution of the nanocomposite is as shown in Figs. 3*a–d*. It is observed that the initiation of damage is in the form of nanosized voids, which are nucleated at the interfaces of two phases (Fig. 3*b*). Growth and coalescence of these nanovoids result in the formation of microcracks (Fig. 3*c*). Then, the microcracks propagate along the interfaces, leading to the final rupture of the nanocomposite (Fig. 3*d*). In the case of $\lambda = 4 \times 10^3$, the initial damage of the nanocomposite is similar to the case of $\lambda = 1$. However, after the nanovoids and microcracks nucleated on the Al/Si interfaces (Fig. 3*e*), they propagate in the Al phase (Figs. 3*f–h*) rather than along the interfaces (Figs. 3*b–d*). The high cohesive energy of the interface is responsible for this discrepancy. In contrast to the above cases, the composite that has a high cohesive parameter (e.g. $\lambda = 7 \times 10^3$) does not exhibit any damage on the interface. The microstructural evolution of this sample under tension is shown in Figs. 3*i–l*. It is noticed that both the nanovoids nucleation and microcracks propagation are mainly located in the Al phase. The underlying deformation mechanisms of the nanocomposite with the highest cohesive parameter $\lambda = 1 \times 10^4$ (Figs. 3*m–p*) is similar to the case of $\lambda = 7 \times 10^3$. However, there is a greater quantity of nanovoids initiated in the Al phase, indicating that the Al phase is much more easily damaged than that in the case of $\lambda = 1 \times 10^4$. It should be noted that there is a lattice mismatch between Al and Si, which can induce misfit dislocation at the interface. The misfit dislocation network at highly mismatched interfaces usually acts as lattice dislocation nucleation sources, and may reduce the strength and stiffness of the nanocomposite [33, 45].

3.3. Unit cell model: To theoretically investigate the effective elastic modulus of the IPC, Tuchinskii [46] and Feng *et al.* [4] proposed cubic unit cells in two different ways based on the iso-strain and iso-stress assumption, respectively. In their models, the interface is treated as a layer of zero thickness, which ideally adheres to the two phases. However, with this simplification of the interface, the previous models did not consider the interface effect. Therefore, to better understand the simulation results, we propose a modified unit cell model, as shown in Fig. 4. Both the Al (purple in Fig. 4*a*) and Si (transparent in Fig. 4*a*) phases are present in the unit cell as three mutually orthogonal branches with rectangular cross-sections. The interface perpendicular to the loading direction (parallel to the *x–z* plane) is considered as a third deformable phase, which is individually represented in yellow colour. The interface parallel to the loading direction (parallel to the *x–y* plane or the *y–z* plane) is still modelled as a zero-thickness layer, which makes the adhered two phases obey the iso-strain assumption.

The effective Young's modulus of such a cubic unit cell can be analytically estimated by a parallel–series decomposition method [3]. First, the unit cell is divided into 2×2 sub-cells, as illustrated in Fig. 4*b*. Using the iso-stress assumption, the effective modulus of each sub-cell is calculated. Secondly, the overall modulus can be determined through the sub-cells using the iso-strain assumption.

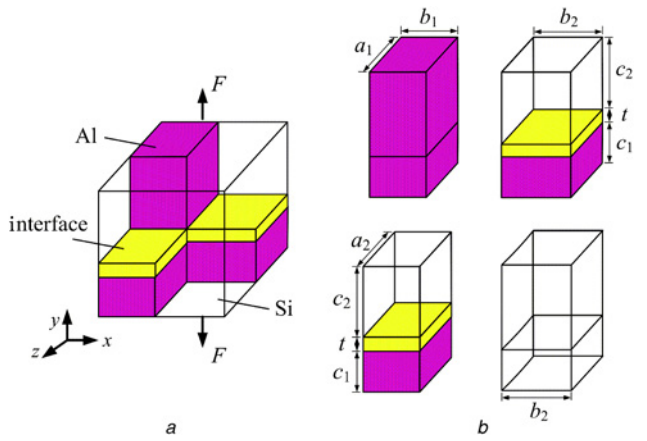

Figure 4 *Unit cell for IPC sample and its decomposition*
a IPC sample
b Its decomposition

On the basis of this method, the effective modulus is given by [4]

$$E = \sum_i \sum_j \left\{ \left[\sum_k \frac{V_{ijk}}{E_{ijk}} \sum_k V_{ijk} \right]^{-1} \sum_k V_{ijk} \right\} \tag{1}$$

where (i, j, k) denotes the serial number of a sub-cell in the three directions, V_{ijk} and E_{ijk} are the volume and Young's modulus of the (i, j, k) sub-cell, respectively. In our cases, we use a simple geometrical relationship $a_1 = b_1 = a$, $a_2 = b_2 = 1 - a$ and $c_1 = c_2 = c = (1 - t)/2$. Then the effective Young's modulus E is derived from (1) as

$$E = a^2 E_a + (1-a)^2 E_s + 2a(1-a)\left(\frac{c}{E_a} + \frac{c}{E_s} + \frac{t}{E_t}\right)^{-1} \tag{2}$$

where E_a, E_s and E_t are the Young's moduli of Al, Si and the interface phase, respectively. It is noted that for a conventional microscale IPC, the thickness of the interface phase $t \to 0$ can be negligible, and (2) reduces to the classical relationship given by Feng *et al.* [4] and Tuchinskii [46].

The Young's modulus of interface phase E_t is related to the parameter λ. Using a continuum model, the interface can be regarded as two parallel planes with a distance h between the two phases. The atoms on the parallel planes are homogenised and represented by an average area density ρ, and the interaction between the two phases is described by the LJ potential. The cohesive energy per unit area of this interface is denoted as $\phi = 4\pi\rho^2\lambda_0\sigma_0^6\left(\sigma_0^6 h^{-10}/5 - h^{-4}/2\right)$ [47]. For this system, the Young's modulus in the direction perpendicular to planes can be estimated as

$$E_t = \frac{\partial(\partial\phi/\partial h)}{\partial h/h} \propto \lambda \tag{3}$$

From (2) and (3), the dependence of Young's modulus E on the cohesive parameter λ is derived as

$$E = D_1 + D_2\left(1 + \frac{D_3}{\lambda}\right)^{-1} \tag{4}$$

where D_1, D_2 and D_3 are the material constants to be determined by experiments or theoretical calculations. Fitting our simulation results by (4) leads to $D_1 = 35.1$ GPa, $D_2 = 55.4$ GPa and $D_3 = 957.4$. The cohesive parameter influences the stiffness of the interface zone, and in turn changes the effective Young's modulus of the IPC. When λ is equal to zero, the overall Young's modulus of the IPC is $E = D_1$. As λ increases, E approaches to a constant value $E = D_1 + D_2$, as shown in Fig. 2*a*.

The ultimate strength is also affected by the parameter λ. In the case of $\lambda < \lambda_c$, the failure of the nanocomposite is mainly attributed to the damage of the interface. With the increase of λ, more energy is required to segregate the interfaces during failure, which results in a higher ultimate strength. After λ exceeds a critical value λ_c, the dominant failure mechanism varies from the damage of the interface to the failure of the weak phase. Using the model in Fig. 4 with an iso-stress assumption, the strain of Al phase ε_a in an Al–Si sub-cell is

$$\varepsilon_a = \left(2 + \frac{t}{c}\right)\left(1 + \frac{E_a}{E_s} + \frac{t}{c}\frac{E_a}{E_t}\right)^{-1} \varepsilon_{sub} \tag{5}$$

where ε_{sub} is the applied strain of the sub-cell. The variations of σ_u with respect to λ can be understood as follows. As λ increases, the Young's modulus of the interface phase E_t increases. For IPC samples with different values of E_t under the same applied strain ε_{sub}, higher E_t means larger ε_a, indicating that the Al phase in the sample with a higher cohesive strength is much more easily damaged.

4. Conclusion: In summary, the tensile deformation behaviours and interfacial effects of interpenetrating phase nanocomposites have been investigated using MD simulations. It is found that as the cohesive energy and cohesive strength of the interface increases, the failure mechanisms of IPCs is varied from the damage of the interface to the failure of the weak phase. The competition of these two mechanisms leads to an optimal cohesive parameter at which the composite has the maximum ultimate strength. A unit cell model is developed to theoretically estimate the nonlinear dependence of the overall Young's modulus on its cohesive parameter. The interface effect on the ultimate strength of nanocomposites is also examined by this model, and we found that the weak phase is much more easily damaged in the nanocomposite which has a higher cohesive energy interface. This study is helpful not only for understanding the physical properties of nanocomposites but also for providing a practical guide for their application.

5. Acknowledgments: This work was supported by the Open Research Fund Program (2042014kf0002) of Wuhan University, the National Natural Science Foundation of China (Grant no. 11372230), and by the Open Research Fund Program (HBKLWJ-2014F02) of the Key Laboratory of Hubei Province for Water Jet Theory and Technology.

6 References

[1] Hamed E., Novitskaya E., Li J., Chen P.Y., Jasiuk I., McKittrick J.: 'Elastic moduli of untreated, demineralized and deproteinized cortical bone: validation of a theoretical model of bone as an interpenetrating composite material', *Acta Biomater.*, 2012, **8**, pp. 1080–1092
[2] Chen Y., Wang A., Fu H., *ET AL.*: 'Preparation, microstructure and deformation behavior of Zr-based metallic glass/porous SiC interpenetrating phase composites', *Mat. Sci. Eng. A, Struct.*, 2011, **530**, pp. 15–20
[3] Feng X.Q., Tian Z., Liu Y.H., Yu S.W.: 'Effective elastic and plastic properties of interpenetrating multiphase composites', *Appl. Compos. Mater.*, 2004, **11**, pp. 33–55
[4] Feng X.Q., Mai Y.W., Qin Q.H.: 'A micromechanical model for interpenetrating multiphase composites', *Comput. Mater. Sci.*, 2003, **28**, pp. 486–493
[5] Wegner L.D., Gibson L.J.: 'The mechanical behaviour of interpenetrating phase composites – II: a case study of a three-dimensionally printed material', *Int. J. Mech. Sci.*, 2000, **42**, (5), pp. 943–964
[6] Wang H., Liao Y., Chao Y., Liang X.: 'Shrinkage and strength characterization of an alumina–glass interpenetrating phase composite for dental use', *Dent. Mater.*, 2007, **23**, pp. 1108–1113

doi: 10.1049/mnl.2014.0304

[7] San Marchi C., Kouzeli M., Rao R., Lewis J.A., Dunand D.C.: 'Alumina–aluminum interpenetrating-phase composites with three-dimensional periodic architecture', *Scripta Mater.*, 2003, **49**, pp. 861–866

[8] Sun Y., Zhang H.F., Wang A.M., *ET AL.*: 'Mg-based metallic glass/titanium interpenetrating phase composite with high mechanical performance', *Appl. Phys. Lett.*, 2009, **95**, p. 171910

[9] Melcher R., Travitzky N., Zollfrank C., Greil P.: '3D printing of Al2O3/Cu–O interpenetrating phase composite', *J. Mater. Sci.*, 2010, **46**, pp. 1203–1210

[10] Tianchi W., Dangsheng X., Tianle Z.: 'Preparation and wear behavior of carbon/epoxy resin composites with an interpenetrating network structure derived from natural sponge', *Carbon*, 2010, **48**, pp. 2435–2441

[11] Lee J.H., Wang L., Boyce M.C., Thomas E.L.: 'Periodic bicontinuous composites for high specific energy absorption', *Nano Lett.*, 2012, **12**, pp. 4392–4396

[12] Poniznik Z., Salit V., Basista M., Gross D.: 'Effective elastic properties of interpenetrating phase composites', *Comput. Mater. Sci.*, 2008, **44**, pp. 813–820

[13] Agarwal A., Singh I.V., Mishra B.K.: 'Evaluation of elastic properties of interpenetrating phase composites by mesh-free method', *J. Compos. Mater.*, 2012, **47**, pp. 1407–1423

[14] Wegner L.D., Gibson L.J.: 'The fracture toughness behaviour of interpenetrating phase composites', *Int. J. Mech. Sci.*, 2001, **43**, pp. 1771–1791

[15] Chandra N., Li H., Shet C., Ghonem H.: 'Some issues in the application of cohesive zone models for metal–ceramic interfaces', *Int. J. Solids Struct.*, 2002, **39**, pp. 2827–2855

[16] Xie D., Waas A.M.: 'Discrete cohesive zone model for mixed-mode fracture using finite element analysis', *Eng. Fract. Mech.*, 2006, **73**, pp. 1783–1796

[17] Freed Y., Banks-Sills L.: 'A new cohesive zone model for mixed mode interface fracture in bimaterials', *Eng. Fract. Mech.*, 2008, **75**, pp. 4583–4593

[18] Harris S.J., O'Neill A., Boileau J., Donlon W., Su X., Majumdar B.S.: 'Application of the Raman technique to measure stress states in individual Si particles in a cast Al–Si alloy', *Acta Mater.*, 2007, **55**, pp. 1681–1693

[19] Noreyan A., Qi Y., Stoilov V.: 'Critical shear stresses at aluminum–silicon interfaces', *Acta Mater.*, 2008, **56**, pp. 3461–3469

[20] Crowson D.A., Farkas D., Corcoran S.G.: 'Mechanical stability of nanoporous metals with small ligament sizes', *Scripta Mater.*, 2009, **61**, pp. 497–499

[21] Crowson D.A., Farkas D., Corcoran S.G.: 'Geometric relaxation of nanoporous metals: the role of surface relaxation', *Scripta Mater.*, 2007, **56**, pp. 919–922

[22] Crowson D.A.: 'Stability of nanoporous metals', PhD thesis, Virginia Polytechnic Institute and State University, 2006

[23] Pugh D.V.: 'Nanoporous platinum', PhD thesis, Virginia Polytechnic Institute and State University, 2003

[24] Cahn J.W., Hilliard J.E.: 'Free energy of a nonuniform system', *J. Chem. Phys.*, 1958, **28**, pp. 258–267

[25] Sun X.Y., Xu G.K., Li X., Feng X.Q., Gao H.J.: 'Mechanical properties and scaling laws of nanoporous gold', *J. Appl. Phys.*, 2013, **113**, p. 023505

[26] Plimpton S.: 'Fast parallel algorithms for short–range molecular dynamics', *J. Comput. Phys.*, 1995, **117**, pp. 1–19

[27] Cao A., Wei Y.: 'Atomistic simulations of the mechanical behavior of fivefold twinned nanowires', *Phys. Rev. B*, 2006, **74**, p. 214108

[28] Tersoff J.: 'New empirical approach for the structure and energy of covalent systems', *Phys. Rev. B*, 1988, **37**, p. 6991

[29] Zope R.R., Mishin Y.: 'Interatomic potentials for atomistic simulations of the Ti–Al system', *Phys. Rev. B*, 2003, **68**, p. 024102

[30] Zulfiqar S., Shah S.I., Sarwar M.I.: 'High clarity, thermally stable and mechanically robust titania nanocomposites: probing the role of binding agent', *Ind. Eng. Chem. Res.*, 2013, **52**, pp. 11050–11060

[31] Gall K., Horstemeyer M.F., Van Schilfgaarde M., Baskes M.I.: 'Atomistic simulations on the tensile debonding of an aluminum–silicon interface', *J. Mech. Phys. Solids*, 2000, **48**, pp. 2183–2212

[32] Noreyan A., Qi Y., Stoilov V.: 'Critical shear stresses at aluminum–silicon interfaces', *Acta Mater.*, 2008, **56**, pp. 3461–3469

[33] Ward D.K., Curtin W.A., Qi Y.: 'Mechanical behavior of aluminum–silicon nanocomposites: a molecular dynamics study', *Acta Mater.*, 2006, **54**, pp. 4441–4451

[34] Dongare A.M., LaMattina B., Irving D.L., Rajendran A.M., Zikry M. A., Brenner D.W.: 'An angular-dependent embedded atom method (A-EAM) interatomic potential to model thermodynamic and mechanical behavior of Al/Si composite materials', *Model. Simul. Mater. Sci. Eng.*, 2012, **20**, p. 035007

[35] Dongare A.M., LaMattina B., Rajendran A.M.: 'Strengthening behavior and tension–compression strength – asymmetry in nanocrystalline metal–ceramic composites', *J. Eng. Mater. Technol.*, 2012, **134**, p. 041003

[36] Peng P., Liao G., Shi T., Tang Z., Gao Y.: 'Molecular dynamic simulations of nanoindentation in aluminum thin film on silicon substrate', *Appl. Surf. Sci.*, 2010, **256**, pp. 6284–6290

[37] Yang Z., Lu Z.: 'Atomistic simulation of the mechanical behaviors of co-continuous Cu/SiC nanocomposites', *Compos. B, Eng.*, 2013, **44**, pp. 453–457

[38] Ding J., Jiang N., Kan B., Cheng G., Yuan N.: 'Interactions between copper and silicon nanofilms with nanogap: a molecular dynamics investigation', *J. Comput. Theor. Nanosci.*, 2012, **9**, pp. 957–962

[39] Jiang L.Y., Huang Y., Jiang H., *ET AL.*: 'A cohesive law for carbon nanotube/polymer interfaces based on the van der Waals force', *J. Mech. Phys. Solids*, 2006, **54**, pp. 2436–2452

[40] Lu W.B., Wu J., Jiang L.Y., Huang Y., Hwang K.C., Liu B.: 'A cohesive law for multi-wall carbon nanotubes', *Phil. Mag.*, 2007, **87**, pp. 2221–2232

[41] Sun X.Y., Li Q., Gu Y., Feng X.Q.: 'Mechanical properties of bioinspired bicontinuous nanocomposites', *Comput. Mater. Sci.*, 2013, **80**, pp. 71–78

[42] Chien C.W., Lee S.L., Lin J.C., Jahn M.T.: 'Effects of Si_p size and volume fraction on properties of Al/Si_p composites', *Mater. Lett.*, 2002, **52**, pp. 334–341

[43] Chien C.W., Lee S.L., Lin J.C.: 'Processing and properties of high volume fraction aluminium/silicon composites', *Mater. Sci. Technol.*, 2003, **19**, pp. 1231–1234

[44] Zhang Q., Zhang H., Gu M., Jin Y.: 'Studies on the fracture and flexural strength of Al/Si_p composite', *Mater. Lett.*, 2004, **58**, pp. 3545–3550

[45] Shao S., Wang J., Misra A., Hoagland R.G.: 'Spiral patterns of dislocations at nodes in (111) semi-coherent FCC interfaces', *Sci. Rep.*, 2013, **3**, p. 2448

[46] Tuchinskii L.I.: 'Elastic constants of pseudoalloys with a skeletal structure', *Powder Metal. Met. Ceram.*, 1983, **22**, pp. 588–595

[47] Zhao J., Jiang J.W., Jia Y., Guo W.L., Rabczuk T.: 'A theoretical analysis of cohesive energy between carbon nanotubes, graphene and substrates', *Carbon*, 2013, **57**, pp. 108–119